Article

Temperature induced monoclinic to orthorhombic phase transition in protonated ZSM-5 zeolites with different Si/Al ratios: An in-situ synchrotron X-ray powder diffraction study

Precisvalle Nicola[1]*, Mancinelli Maura[1], Ardit Matteo[1], Beltrami Giada[1], Gigli Lara[2], Aloise Alfredo[3], Catizzone Enrico[4], Massimo Migliori[4], Giordano Girolamo[4], Guidi Vincenzo[1], and Annalisa Martucci[1]*

[1] Physics and Earth Science Department, University of Ferrara, via Saragat 1, I-44122 Ferrara, Italy

[2] Materials Characterization by X-ray diffraction (MCX) beamline, Elettra-Sincrotrone Trieste S.C.p.A., SS14-km 163,5 Science Park AREA, I-34149 Basovizza, Italy

[3] Department of Physical and Chemical Sciences, University of L'Aquila, Via Vetoio (COPPITO 1–2), 67100 L'Aquila, Italy.

[4] Department of Environmental and Chemical Engineering, University of Calabria, via Bucci Cubo 44a, I-87036 Rende, Italy

*Corresponding author(s): Nicola Precisvalle (prcncl@unife.it) and Annalisa Martucci (mrs@unife.it)

Abstract: ZSM-5 zeolite is the synthetic counterpart to mutinaite. After thermal activation of the as-synthesized form, the symmetry of the ZSM-5 zeolite is lowered to the monoclinic $P2_1/n$. ZSM-5 then undergoes a polymorphic displacive phase transition from the monoclinic $P2_1/n$ to the orthorhombic $Pnma$, $Pn2_1a$ or $P2_12_12_1$ space groups, which occurs upon heating. This phase transition can be influenced by factors such as the type and amount of sorbate molecules present in the zeolite channels. ZSM-5 has many applications, including as a catalyst or sorbent in various industries, where high thermal stability is required. In this study, four ZSM-5 zeolites with different Si/Al ratios were investigated by synchrotron X-ray powder diffraction at both room temperature and high temperature conditions to determine the effects of chemical composition on the structural response of the zeolite lattice. The results showed that the ZSM-5 zeolites retained their crystallinity and structural features throughout the thermal treatment, indicating that they could be used as effective acid catalysts. Distortions in the zeolite framework can occur after TPA+ decomposition and thermal activation, affecting thermal regeneration and efficiency. The charge balance in ZSM-5 is achieved by the formation of Brønsted acid sites, and variations in bonding geometries are influenced by the initial Si/Al ratio.

Keywords: Zeolite structure, ZSM-5, X-ray powder diffraction, catalyst, acid sites

1. Introduction

Zeolites are amongst the most widely investigated and topical crystalline inorganic microporous solids due to the variable chemical composition of the framework as well as tunable pore size and architecture. These features make them very suitable for a wide range of applications in adsorption, separation, catalysis, microelectronics as well as in any field where the host–guest chemistry defines the final behaviour of the system. [1–3] The pores defined by the peculiar organization of the corner-sharing [TO4] tetrahedra are open to the external surface allowing the mass transfer from the exterior toward the interior of the particle provided that the size of the molecule is smaller than the dimensions of the pores. As a consequence, different pores dimensions with a well-defined structure make zeolites excellent shape selective materials. The presence of extraframework charge-

compensating cations and acid sites confer to them enhanced catalytic properties. The possibility to modify both type and location of extraframework cations through ion exchange processes control and influence both their selectivity and catalytic activity.[4,5] Besides, the hydrophobic or hydrophilic nature is fundamental in determining the zeolites sorption properties towards specific organic compounds from gas phase or water solution. Zeolites play an important role in that called sustainable processes, such as the field of renewable energy and environmental remediation[6,7] In the field of renewable energy, these materials are principally studied for biomass conversion, fuel cells, thermal energy storage, CO_2 capture and conversion.[8–12] Additionally, for environmental remediation processes zeolites are mainly used for out-door air quality monitoring, water and wastewater purification from heavy metals and organic compounds of different nature, etc.[13–17] ZSM-5 zeolite is the synthetic counterpart of the mutinaite mineral, $(Na_{2.76}K_{0.11}Mg_{0.21}Ca_{3.78})(Al_{11.20}Si_{84.91})\cdot 60H_2O$ [18], characterized by a high content of Na and especially Ca extraframework cations. ZSM-5 belongs to the so-called pentasil zeolite class with a MFI framework topology and a 3-dimensional channel system. [19,20] The ideal chemical formula of ZSM-5 is $(Na^+_n)[Al_nSi_{96-n}O_{192}]\cdot(H_2O)_{16}$, n<27 [21]. Its crystal structure can be rationalized as the intersection of two sets of tubular channels, both defined by a 10-membered ring: the straight channel (SC) parallel to the [010] direction, and the sinusoidal channel (ZZ) parallel to the [100] direction. The opening of SC and ZZ channels, expressed by their free diameter, ranges from 5.4 to 5.6 Å and from 5.1 to 5.5 Å, respectively [22]. The topological symmetry of the as-synthesized ZSM-5 (*i.e.,* with template molecules in the channel system) is the orthorhombic *Pnma* defined by 12 tetrahedral sites per unit cell and lattice parameters at ambient conditions of *a* = 20.09(1), *b* = 19.73(1), and *c* = 13.14(1) Å. [23,24] After thermal activation of the as-synthesized form, the symmetry of the ZSM-5 zeolite is lowered to the monoclinic *P*2$_1$/*n*. [24] Thermal activation is a well-known treatment that promotes protonation of as-synthesized ZSM-5 and confers catalytic properties, resulting in ZSM-5c zeolites. [24] ZSM-5c zeolites undergo a polymorphic displacive phase transition from the monoclinic *P*2$_1$/*n* to the orthorhombic *Pnma*, *Pn*2$_1$*a* or *P*2$_1$2$_1$2$_1$ space groups (*i.e.,* *m*➔*o*) that occurs upon heating. [22,25–29] The *m*➔*o* phase transition is induced by several factors, such as the type and amount of sorbate molecules when present in the zeolite channels. The nature of this *m*➔*o* phase transition was recently investigated by [30,31] through the analysis of the spontaneous strain variation on a high-silica ZSM-5 hydrophobic zeolite (Si/Al ratio = 140). ZSM-5c is a ferroelastic material that exhibits a polymorphic phase transition (from the ferroelastic monoclinic to the paraelastic orthorhombic phase) with a tricritical character. [30,31] Analysis of the thermodynamic properties of the *m*➔*o* phase transition probed that the transition temperature and its thermodynamic features strongly depend on the Si/Al ratio, as well as the different nature of encapsulated organic compounds and host-guest interactions. Due to the unique structural features and physiochemical properties (i.e., solid acidity, shape selectivity, pore size, thermal/mechanical/ chemical stability and regenerability), ZSM-5 has widespread applications in petrochemical processing, fine chemical production, liquid and gas separation in oil refinery, petrochemical industry, and environmental catalysis.[32–34] Besides, ZSM-5 exhibits excellent catalytic properties in the Fluid Catalytic Cracking (FCC) process to improve gas octane number and the selectivity of light olefins[7,35] as well as in aromatics compounds synthesis due to its shape-selective medium-pore.[36,37] When used in water treatment plants, ZSM-5 has recently shown good performance in the adsorption of organic compounds of different nature, such as DCE (1,2-dichloroethane), BTEX (benzene, toluene, ethyl benzene and xylenes) and methyl tertiary butyl ether (MTBE), pollutants that have harmful effects on human health and ecosystems. [38–41] Either as a catalyst or in water remediation plants, the main requirement for ZSM-5 is a high thermal stability. Catalytic reactions are usually carried out in a wide temperature range, which can reach 500-600 °C, while the regeneration of zeolites is usually achieved by thermal treatment up to 600-800 °C. It follows that the prediction of the thermally induced structural evolution of ZSM-5 is one of the key issues to characterize these

Commentato [MA1]: (Rimer, J. D. (2018). Rational design of zeolite catalysts. Nature Catalysis, 1(7), 488-489; Čejka, J., Millini, R., Opanasenko, M., Serrano, D. P., & Roth, W. J. (2020). Advances and challenges in zeolite synthesis and catalysis. Catalysis Today, 345, 2-13).

Commentato [MA2]: Kausar, A., Ahmad, I., Zhu, T., Shahzad, H., & Eisa, M. H. (2023). Exigency for the Control and Upgradation of Indoor Air Quality—Forefront Advancements Using Nanomaterials. Pollutants, 3(1), 123-149; Ziejewska, C., Grela, A., Łach, M., Marczyk, J., Hordyńska, N., Szechyńska-Hebda, M., & Hebda, M. (2023). Eco-friendly zeolites for innovative purification of water from cationic dye and heavy metal ions. Journal of Cleaner Production, 406, 136947; Mancinelli, M., Stevanin, C., Ardit, M., Chenet, T., Pasti, L., & Martucci, A. (2022). PFAS as emerging pollutants in the environment: A challenge with FAU type and silver-FAU exchanged zeolites for their removal from water. Journal of Environmental Chemical Engineering, 10(4), 108026; Mahdavi Far, R., Van der Bruggen, B., Verliefde, A., & Cornelissen, E. (2022). A review of zeolite materials used in membranes for water purification: History, applications, challenges and future trends. Journal of Chemical Technology & Biotechnology, 97(3), 575-596; Panasenko, A. E., Shichalin, O. O., Yarusova, S. B., Ivanets, A. I., Belov, A. A., Dran'kov, A. N., ... & Papynov, E. K. (2022). A novel approach for rice straw agricultural waste utilization: Synthesis of solid aluminosilicate matrices for cesium immobilization. Nuclear Engineering and Technology, 54(9), 3250-3259

Commentato [MA3]: Louwen, J. N., Van Eijck, L., Vogt, C., & Vogt, E. T. (2020). Understanding the activation of ZSM-5 by phosphorus: localizing phosphate groups in the pores of phosphate-stabilized ZSM-5. *Chemistry of Materials, 32(21), 9390-9403.*

microporous compounds. [24,42,43] Indeed, these studies return to be fundamentals to prevent a possible catalyst deactivation from one side or a possible framework distortion affecting the thermal regeneration and the efficiency of the ZSM-5 zeolite after the treatment. In this work, four ZSM-5c zeolites, belonging to the same synthesis batch and characterized by a different Si/Al ratio are investigated by synchrotron X-ray powder diffraction at high temperature (*HT*). A whole structural characterization at room temperature (*RT*) as well as at *HT* conditions will shed light on the differences and similarities among the four samples to determine the effects of the different chemical composition on the ZSM-5 structural response to the heating process.

2. Materials and Methods

Zeolites. The samples used in this work are four synthetic protonated ZSM-5c zeolites (*i.e.*, MFI topology, 3-dimensional channels system) characterized by different Si/Al ratio. All samples have been synthesized and provided by the research group of the Department of Chemical and Environmental Engineering of the University of Calabria (Rende, CS) using the synthesis procedure reported by Migliori et al. (2014)[44]. Differences in Si/Al ratio are due to the different amount of Al_2O_3 used in the molar composition of the starting gel. [45] The sample labels along with the corresponding Si/Al ratio are listed in Table 1.

Table 1.

Label, bulk Si/Al ratio, and Al^{+3} content of each ZSM-5 sample.

Sample label	Bulk Si/Al ratio [mol/mol]	Al content (apfu)
ZSM-5c_15	15	6.19
ZSM-5c_20	20	4.57
ZSM-5c_37	37	2.53
ZSM-5c_69	69	1.37

Synchrotron X-ray Powder Diffraction. *In situ* high temperature diffraction patterns were collected at the MCX (Material Characterization by X-ray Diffraction) beamline of the Elettra Synchrotron Light Source (Trieste, Italy) on a 4-circle Huber diffractometer with a 3D translation sample stage. The diffractometer was equipped a high-count rate fast scintillator detector, preceded by a pair of slits with vertical apertures of 200 and 300 μm. Powder samples were placed in a spinning quartz capillary (∅ = 0.5 mm) previously mounted on a goniometric head rotating along the axis of the diffractometer. X-ray diffraction patterns were recorded from *RT* to a maximum temperature of 800 °C according to the following experimental conditions: every 100 °C with a heating rate of 5 °C min^{-1}, fixed wavelength of 0.82700(1) Å (photon energy of 15 keV) in the range 3–45° 2θ, with a step size of 0.005° 2θ and an exposure time of 1 second per step. Figure 1 shows a comparison of the X-ray diffraction patterns collected.

Refinement Strategy. Full profile Rietveld refinements were performed using the GSAS software and the EXPGUI graphical interface. [46,47] The *RT* diffraction data of ZSM-5c with Si/Al ratio equal to 20, 37, and 69, respectively, were refined in the monoclinic crystal system (space group $P2_1/n$), starting from the structural model reported by [24], while the sample with the Si/Al ratio = 15 was refined in the orthorhombic *Pnma* symmetry, starting from the atomic coordinates of [23]. At higher temperatures (*i.e.,* between 100 and 800 °C), all the structural refinements were carried out in the orthorhombic crystal system (space group *Pnma*). In all refinements, the peak profiles were modelled by a pseudo-Voigt function with the peak cut-off set to 0.01% of the peak maximum, three Gaussian terms (θ-independent *GW*, tan^2-θ and tan-θ dependent *GU* and *GV*, respectively), the Lorentzian

---

Commentato [MA4]: *Migliori, M., Aloise, A., & Giordano, G. (2014). Methanol to dimethylether on H-MFI catalyst: The influence of the Si/Al ratio on kinetic parameters. Catalysis Today, 227, 138-143*

Commentato [l5]: Mancano le refernze della linea le metterei entrambe se non è un problema: **The X-ray diffraction beamline MCX at Elettra: a case study of non-destructive analysis on stained glass**
Plaisier Jasper Rikkert, Nodari Luca, Gigli Lara, Rebollo San Miguel Elena Paz, Bertoncello Renzo, Lausi Andrea
ACTA IMEKO, Vol. 6 - 3, pp. 71-75 (2017)
doi: 10.21014/acta_imeko.v6i3.464

MCX: A synchrotron radiation beamline for X-ray diffraction line profile analysis
Rebuffi L, Plaisier JR, Abdellatief M, Lausi A, Scardi P
Zeitschrift fur Anorganische und Allgemeine Chemie **640** 3100–3106. *(2014).*
doi: 10.1002/zaac.201400163

Commentato [l6]: Per il futuro: il double crystal monochromator è il monocromatore della linea e non sta sul diffrattometro, forse volevi dire più cose della linea ma è venuto fuori questo. Quindi ho tolto quella parte e lasciato il resto che è corretto.

Commentato [l7]: Il terzo reviewer dice:
Please elaborate on the parameters of the synchrotron detector
(/10.1016/j.ceramint.2022.03.068)
Sinceramente non capisco cosa vuole forse non sa cos'è un scintillator detector, ho guardato il paper che nomina e probabilmente è il suo o di amici.

Commentato [l8]: Siamo sicuri? non è un mio classico valore di raccolta, controlla perfavore, di solito io faccio o suggerisco 0.008°

cosθ^{-1}-dependent *LX* coefficient and an asymmetry (*asym*) contribution. The experimental
background was fitted by 28 shifted Chebyshev polynomial coefficients. Refinements also
included lattice parameters, framework atomic coordinates, and atomic displacement pa-
rameters (ADPs, U$_{iso}$). Soft constraints were applied to the tetrahedral T–O and O–O bond
distances (1.60 and 2.60 Å, respectively, with σ = 0.04 Å). The restraint weight (F) was
progressively reduced in the final refinement cycles until the atomic coordinates were al-
lowed to vary almost freely. In addition, the U$_{iso}$ parameters of tetrahedral sites and frame-
work oxygen atoms were constrained to have the same value for the same atomic species.
The lattice parameters and unit-cell volumes obtained by full profile Rietveld refinements,
as well as the *R*-value agreement indices of the investigated samples, are listed in Table 2.

Table 2.

Lattice parameters, data collection details, and R-value agreement indices at room temperature.

Parameter	ZSM-5c_15	ZSM-5c_20	ZSM-5c_37	ZSM-5c_69
Space Group	*Pnma*	*P2$_1$/n*	*P2$_1$/n*	*P2$_1$/n*
a (Å)	20.1464(11)	19.9413(9)	19.9119(11)	19.9108(5)
b (Å)	19.9434(10)	20.1503(8)	20.1321(11)	20.1319(4)
c (Å)	13.4168(9)	13.4167(6)	13.3952(8)	13.3943(4)
V (Å³)	5390.7(5)	5391.0(4)	5369.5(5)	5368.7(2)
β (°)	90	90.354(4)	90.477(2)	90.499(1)
Wavelength (Å)	0.82700(1)	0.82700(1)	0.82700(1)	0.82700(1)
2θ (°) range	3-45	3-45	3-45	3-45
N$_{data}$	8400	8400	8400	8400
N$_{var}$	117	256	256	256
R$_{wp}$ (%)	12.88	13.23	13.84	9.45
R$_p$ (%)	9.28	9.98	10.99	7.36
R$_F$ (%)	9.48	8.08	8.2	4.72
R$_F{}^2$ (%)	10.58	13.00	12.01	7.23

$$\mathbf{R_p = \sum[Y_{io} - Y_{ic}]/\sum Y\_{io}; \; R_{wp} = [\sum wi(Y_{io} - Y_{ic})^2/\sum wiY_{io}^2]^{0.5}; \; R_F{}^2 = \sum|F_o^2 - F_c^2|/|F_o^2|}$$

Framework atomic coordinates, atomic fractions, and ADPs of the samples at room tem-
perature are reported as supplemental information in Tables SI1-SI4. Framework atomic
coordinates, atomic fractions, and ADPs at selected temperatures of 200, 400, 600 and 800
°C are reported as supplemental information in Tables SI5-SI8, SI9-SI12, SI13-SI16, and
SI17-SI20 for samples ZSM-5c_15, ZSM-5c_20, ZSM-5c_37, and ZSM-5c_69, respectively.

3. Results and Discussion

The discussion is conceived in two distinct sections. The first is devoted to the structural
characterization of the H$^+$-ZSM-5 samples at RT, while the second is devoted to the deter-
mination of the structural evolution at HT (i.e., at temperatures higher than 100 °C, after
the occurrence of the monoclinic to orthorhombic phase transition).

#### 3.1. *Structural Characterization*

3.1.1 Room temperature

Peak indexing of the collected powder diffraction pattern at *RT* shows that for sample ZSM-5c_15 the characteristic doublets of the monoclinic polymorph peaks (*i.e.*, [311], [-313], and [313]) are not fully resolved. In fact, the peaks centred at about 8.5 and 13.1° 2θ are broader and more intense than those of the other samples due to a possible convolution of more peaks (Figure 1).
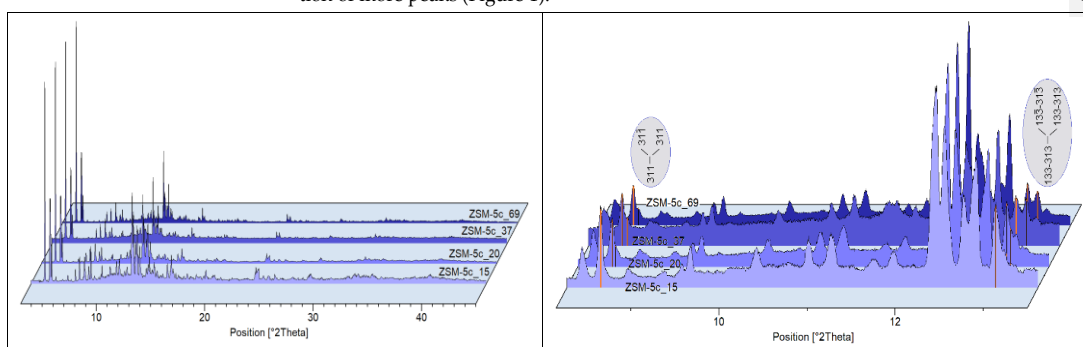

Figure 1. Comparison of the powder diffraction patterns of all ZSM-5 samples in the entire angle range investigated (left) and in the angle range 8.0-14.0° 2θ (right). The characteristic doublet of monoclinic phase peaks at room temperature becomes a broad single peak for the sample ZSM-5c_15, characteristic of the orthorhombic polymorph.

An attempt at structural refinement in the monoclinic $P2_1/n$ space group gives a β angle very close to 90° with relatively unsatisfactory refinement agreement factors (*i.e.*, R_{wp}=18.69%, R_p=14.43%, R_t=18.70% and R_{F^2}=23.12%). For these reasons, the Rietveld refinement of the ZSM-5c_15 sample was performed in the orthorhombic *Pnma* space group at each temperature studied. The refinement agreement indices, as reported in Table 2 for the structure refinement at *RT*, result improved and comparable to those of the other samples. The structure of ZSM-5c samples with higher Si/Al ratio (ZSM-5c_20, 37 and 69) was successfully resolved by refinement in the monoclinic $P2_1/n$ space group (Table 2). Considering that the activation procedure is the same for all the samples studied, the structural differences are mainly due to differences in their chemical composition (*i.e.*, different Al content). The Si/Al ratio plays a key role in the formation of defects in the zeolite framework and consequently in its structural properties. As highlighted in the case of ZSM-5c single-crystals [48], high Al contents within the zeolite framework cause internal stresses that mainly affect the orientation of the ZSM-5 twin domains. This is reflected in the variation of the β angle, which changes from 90° (orthorhombic) to higher values as a function of increasing Si/Al ratio, thus determining increasing degrees of "monoclinicity". Figure 2 shows the variation of the normalized lattice parameters, the β angle, and the unit-cell volume as a function of increasing Si/Al ratio. Both the normalized *a* and *c* lattice parameters decrease with a similar rate of variation as a function of the Si/Al ratio, while the unit-cell *b*-axis is the less affected by the different chemical composition. Indeed, Figure 2b clearly shows a close relationship between the Al content and the degree of monoclinicity of activated ZSM-5 zeolites, with the β angle ranging from 90 to 90.49°.

A general framework of the ZSM-5c chemical dependence is shown in Figure 2c, where a volumetric decrease occurs with increasing Si/Al ratio. This volumetric change is mainly due to the substitution of Si^{+4} for Al^{+3} at the tetrahedral site of the zeolite framework (the ionic radius of Al^{+3} and Si^{+4} in tetrahedral coordination is equal to 0.39 Å and 0.26 Å, respectively, [49]).
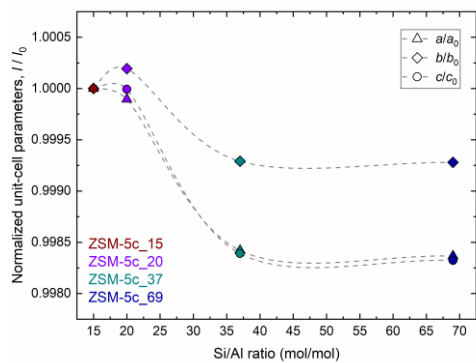
a)
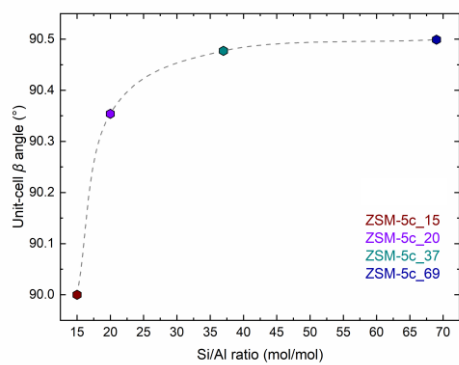
b)
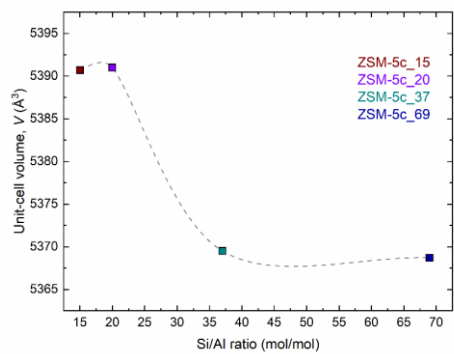
c)

210
211
212
213
214
215
216
217

Figure 2. Lattice parameters (a), β angle (b) and unit-cell volume (c) of the four investigated ZSM-5c zeolite samples as a function of the Si/Al ratio at room temperature. Dashed lines are a reader's guide. Error bars are within the symbol size.

All the ZSM-5c samples investigated here are characterized by a regular framework geometry, with mean tetrahedral bond distances ranging from 1.591 to 1.593 Å.

Regarding the shape and dimension of the channels, the values obtained from the calculation of the ellipticity (ε) and the crystallographic free area (CFA) parameters (Table 3) indicate that the Si/Al ratio also affects the channels opening. In fact, the presence of slight differences in both straight and sinusoidal channels among the four samples suggests that their geometry is already slightly distorted under ambient conditions.

Table 3.

O-O distances and CFA of SC, ZZ-A and ZZ-B channels for the four ZSM-5c samples.

|	Free diameter (Å)								
ZZA	**O28-O1**	**O27-O2**	**O20-O15**	**O24-O26**	**O41-46**	**Mean O-O (Å)**	**Radius (Å)**	**CFA (Å^2)**	**ε**
ZSM-5c_20	5.426	5.447	5.688	5.341	5.794	5.5392	2.7696	24.09	1.08
ZSM-5c_37	5.453	5.443	5.688	5.313	5.808	5.541	2.7705	24.10	1.09
ZSM-5c_69	5.405	5.476	5.651	5.301	5.835	5.5336	2.7668	24.04	1.1
ZSM-5c_15	**O18-O17**	**O18-O17**	**O4-O5**	**O4-O5**	**O25-O23**	**Mean O-O (Å)**	**Radius (Å)**	**CFA (Å^2)**	**ε**
	5.272	5.272	5.325	5.325	5.864	5.411	2.705	22.98	1.11
ZZB	**O31-O4**	**O30-O5**	**O44-O43**	**O25-O23**	**O18-O17**	**Mean O-O (Å)**	**Radius (Å)**	**CFA (Å^2)**	**ε**
ZSM-5c_20	5.233	5.491	5.44	5.853	5.146	5.4326	2.7163	23.17	1.13
ZSM-5c_37	5.163	5.549	5.498	5.498	5.061	5.3538	2.6769	22.50	1.09
ZSM-5c_69	5.145	5.587	5.483	5.822	5.071	5.4216	2.7108	23.07	1.14
ZSM-5c_15	**O1-O2**	**O1-O2**	**O15-O20**	**O15-O20**	**O24-O26**	**Mean O-O (Å)**	**Radius (Å)**	**CFA (Å^2)**	**ε**
	5.451	5.451	5.746	5.746	5.368	5.552	2.776	24.20	1.07
SC	**O47-O48**	**O31-O37**	**O44-O46**	**O8-O2**	**O7-O1**	**Mean O-O (Å)**	**Radius (Å)**	**CFA (Å^2)**	**ε**
ZSM-5c_20	5.425	5.512	5.561	5.399	5.491	5.477	2.738	23.55	1.03
ZSM-5c_37	5.438	5.517	5.929	5.379	5.436	5.539	2.769	24.09	1.10
ZSM-5c_69	5.444	5.554	5.629	5.407	5.409	5.488	2.744	23.65	1.04
	O1-O7	**O2-O8**	**O5-O11**	**O18-O20**	**O21-O22**	**Mean O-O (Å)**	**Radius (Å)**	**CFA (Å^2)**	**ε**
ZSM-5c_15	5.642	5.440	5.621	5.839	5.518	5.511	2.755	23.84	1.07

3.1.2 High Temperature

Examination of the powder diffraction patterns collected at high temperature (*i.e.*, from

100 to 800 °C, each 100 °C) shows that the samples with the higher Si/Al ratio (ZSM-5c_20, 37, and 69) underwent a monoclinic to orthorhombic phase transition for temperatures below 100 °C. All the characteristic peak doublets identified for the monoclinic polymorphs merged into single peaks (Figure 3) and consequently all Rietveld refinements at temperature ≥ 100 °C were performed in the orthorhombic *Pnma* space group.
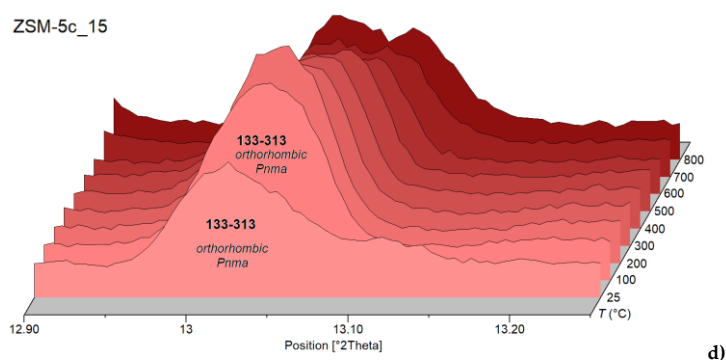

a)

b)

c)

d)
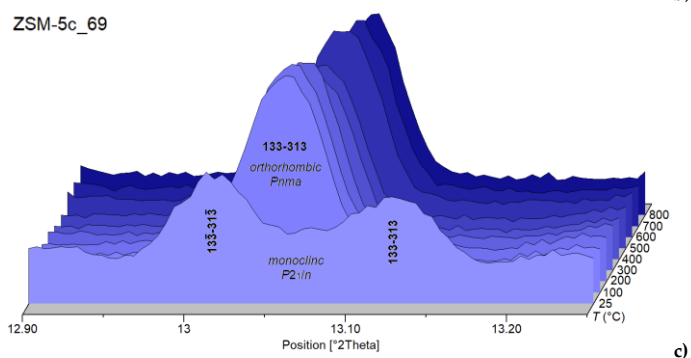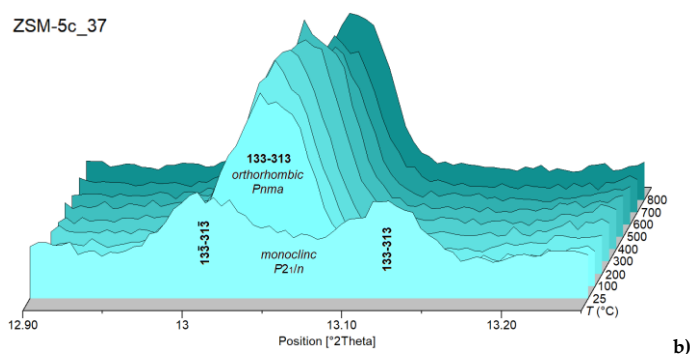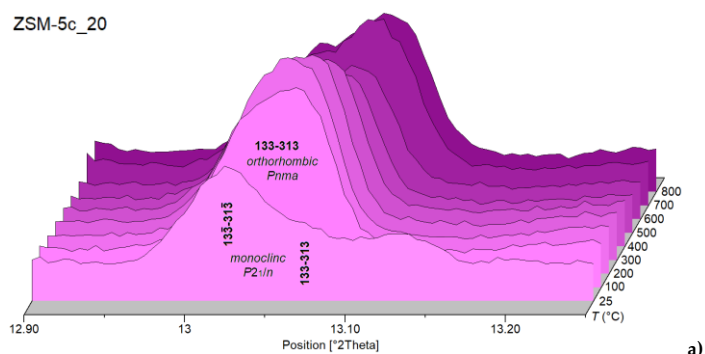
Figure 3. Example of peak merging (the characteristic doublet of monoclinic phase peaks at room temperature becomes a single peak at high temperature, characteristic of the orthorhombic polymorph) for the samples 20 (b), 37 (c) and 69 (d) in the 12.90-13.25° 2θ regions, while the sample ZSM-5c_15 (d) retains the orthorhombic symmetry throughout the investigated thermal range.

The evolution of the powder patterns upon heating is shown in Figure 4 (i.e., details of the high temperature patterns in the 3-10° 2θ and 10-20° of 2θ ranges, respectively). No evidence of crystallinity loss is observed within the investigated temperature range, confirming the high thermal stability typically exhibited by ZSM-5 zeolites.

A comparison of the high temperature evolution of the normalized lattice parameters for the ZSM-5c samples is shown in Figure 5. Despite a remarkable difference in their crystal chemistry (with a Si↔Al substitution varying from 1.4 to 6.2 apfu, Table 1), all the investigated zeolite samples show a common evolution of the lattice parameters with temperature. In fact, after a minimal variation of the lattice parameters between 100 and 200 °C, a common lattice shortening along the crystallographic unit-cell axes is observed.

Up to the maximum investigated temperature, the average lattice shortening for all the ZSM-5c under comparison is equal to 0.3, 0.1, and 0.15% for the unit-cell parameters *a*, *b*, and *c*, respectively, indicating an anisotropic response to the thermal treatment. Noteworthy is the behaviour of the ZSM-5c_69 between 400 and 500 °C along all directions, where no changes in lattice parameters are observed. In addition to reproducing all the features previously described for the lattice parameters, the contraction of the unit-cell volume upon heating (Figure 6) is ascribable to the so-called negative thermal expansion (NTE) phenomenon, which results from the cooperative or supramolecular structural mechanisms prevailing over the positive thermal expansion of interatomic bonds. [50]
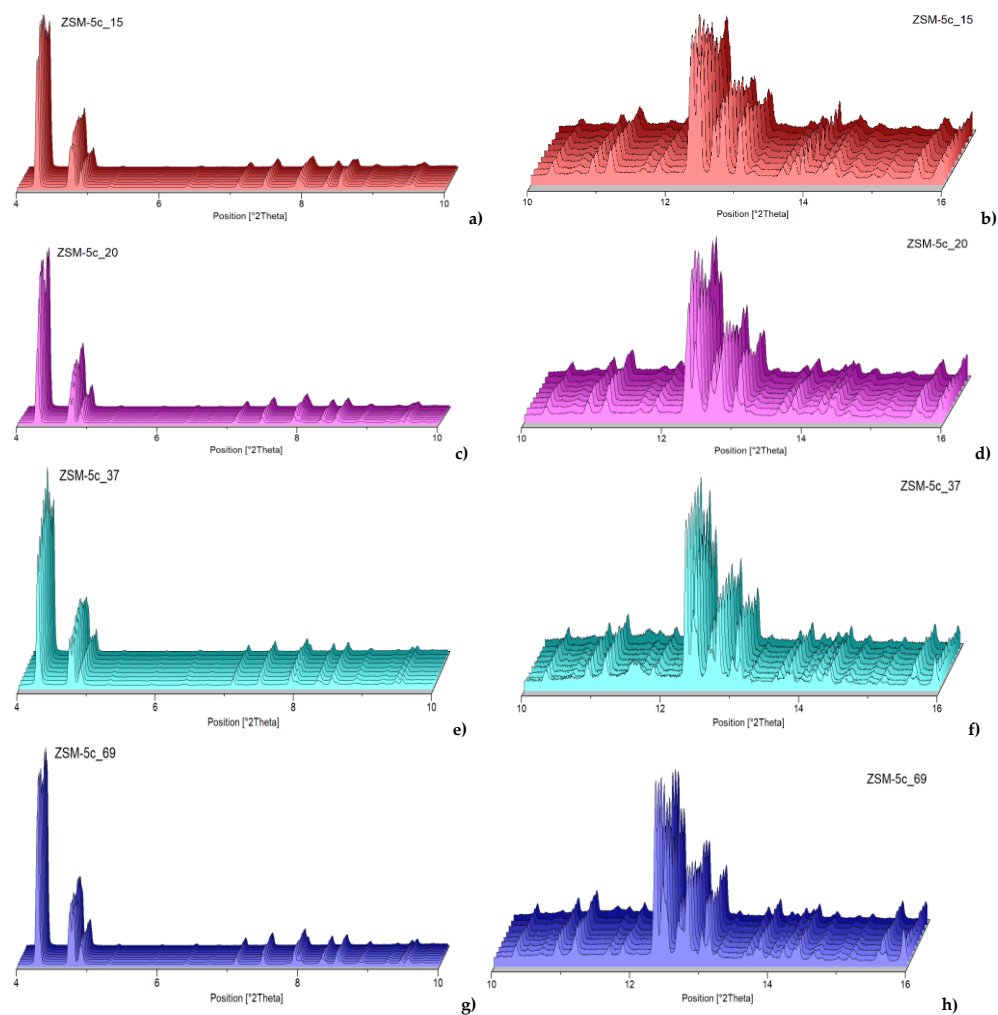
Figure 4. X-ray powder diffraction patterns collected at high temperature (details of low and high 2θ angles) for samples ZSM-5c_15- (a,b), ZSM-5c_20 (c,d), ZSM-5c_37 (e,f) and ZSM-5c_69 (g,h).
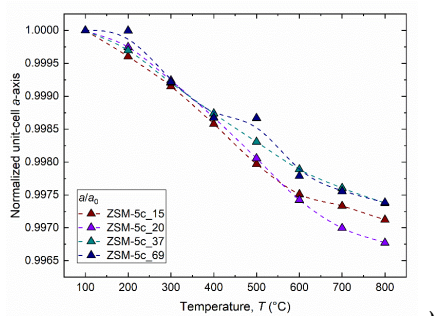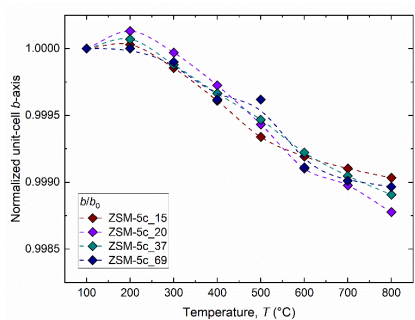
279
280
281
282
283
284
285
286

a)
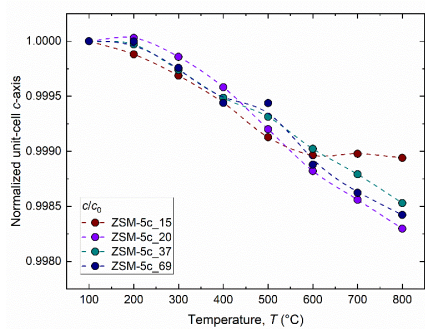
b)

c)

Figure 5. Temperature dependence evolution of the normalized lattice parameters ((a) a/a0, (b) b/b0 and (c) c/c0) for the investigated ZSM-5c samples.

The mean volumetric reduction (δV) calculated on the normalized values is equal to 0.5%, with the exception of sample ZSM-5c_20, which shows a slightly higher variation (*i.e.*, δV = 0.6%).
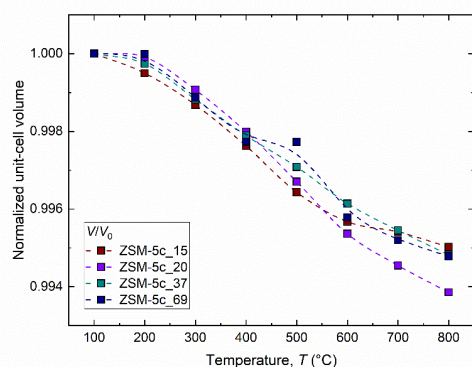
Figure 6. Evolution of the unit cell volume upon heating of the investigated ZSM-5c samples.

To describe the observed NTE phenomenon in a thermodynamic way, the variation of the lattice parameters was rationalized by the Fei polynomial function [51], as implemented in EosFit7c [52], Eq.1:

$$\alpha = \alpha_0 + \alpha_1 T + \alpha_2 T^{-2} \ (T = \text{Kelvin}) \quad (1)$$

where the mean thermal expansion coefficient α is expressed in K^{-1}, while the constants α_0, α_1, and α_2, are expressed in K^{-1}, K^{-2}, and K, respectively. The values obtained by applying Equation 1 to each ZSM-5 sample are listed in Table 4.

Table 4.

Values of constants in Equation 1 (with $\alpha_0 \times 10^{-5}$, $\alpha_1 \times 10^{-8}$, and α_2 in K^{-1}, K^{-2}, and K, respectively) obtained from Fei polynomial fits. $\alpha_{(200-800)}$ ($\times 10^{-6}$ in K^{-1}) is the mean coefficient of thermal expansion between 200 and 800 °C.

	ZSM-5c_15	ZSM-5c_20	ZSM-5c_37	ZSM-5c_69 *
V_0	5373.46(25)	5370.76(34)	5373.46(25)	5368.52(19)
α_0	-2.1(6)	-6.1(9)	-2.1(6)	-4.08(5)
α_1	1.3(5)	4.5(9)	1.3(5)	3.30(4)
α_2	1.4(9)	7.9(9)	1.40(9)	3.35(7)
$\alpha_{V(200-800)}$	-8.21	-10.08	-8.21	-8.67

Note. The data at 500 °C was considered an outlier and was not included in the calculation of the polynomial regression

Although the mean volumetric thermal expansion coefficients calculated between 200 and 800 °C for the investigated samples are quite similar, they are higher than those reported for other zeolites with MFI framework topology. In particular, an $\alpha_{V(150-600)}$ of −6.43 ⊛ 10⁻⁶ K⁻¹ has been reported for a ZSM-5c with a Si/Al ratio of 140 [30], while an $\alpha_{V(150-600)}$ of −7.60 ⊛ 10⁻⁶ K⁻¹ for a sample of silicalite (*i.e.*, Al → 0,[53]).

Figure 7 shows the evolution of the atomic displacements parameters for the cations hosted at the tetrahedral sites between 100 and 800 °C for all the ZSM-5c samples. As reported in

the refinement strategy section, the ADPs were constrained to be isotropic and to change equally for the 12 tetrahedral sites in the unit-cell. The ADPs increase continuously up to the maximum temperature. Since no extraframework species are present in the zeolite pore system, the evolution of ADPs with temperature must be attributed exclusively to atomic thermal motion.
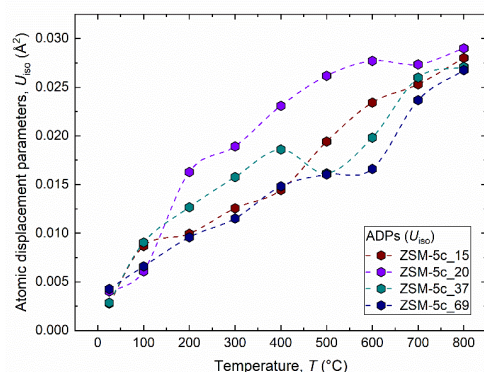

Figure 7. Evolution of ADPs parameters during heating.

Although it might be reasonable to attribute the increase in ADPs to an increase in structural disorder, no direct experimental evidence can be inferred from X-ray powder diffraction for the breaking of T–O–T bonds and the formation of Lewis acid sites. [54] Indeed, the refined T-O bond distances and T-O-T angles at high temperature (reported as supplementary material at 200, 400, 600 and 800 °C for each sample; Tables SI23-SI26 for ZSM-5c_15, ZSM-5c_20, ZSM-5c_37 and ZSM-5c_69, respectively) confirm the high stability and flexibility of the selected catalysts.

No significant variations were observed in the evolution of the ellipticity parameter. In fact, both sinusoidal (ZZ-A and ZZ-B) and straight channels (Figure 8) do not show any evident variation in shape and geometry between 100 and 800 °C, thus proving that the zeolitic framework does not undergo any relevant distortions until the end of the thermal treatment. More specifically, the evolution of the sinusoidal channels (*i.e.*, for both entrance and exit) appears more regular than that of the straight one. Moreover, the ellipticity increases progressively from 100 to 800 °C for all the analyzed samples, although at a low rate. The samples with the lowest Si/Al ratio are characterized by straight channels that follow similar trends: the ellipticity increases progressively (*i.e.*, the point at 500 °C point is not taken into account) up to 800 °C, unlike the samples with the highest Si/Al ratio.
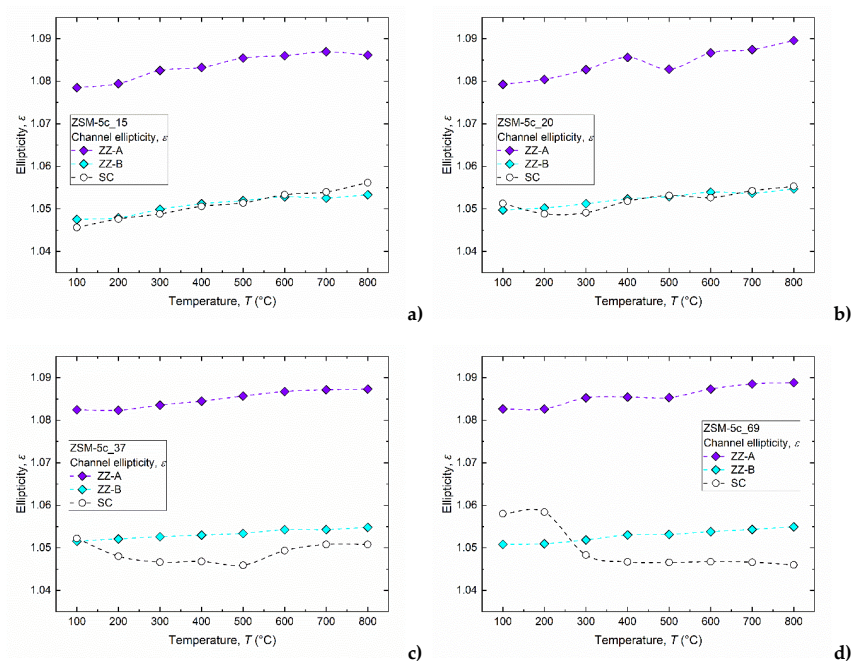
Figure 8. Evolution of the ellipticity parameter with temperature for the four ZSM-5c samples.

(a) ZSM5C_15; (b) ZSM5C_20, (c) ZSM5C_37 and (d) ZSM5C_69

Structural density, on the other hand, presents a different behavior related to the SAR. Looking the SAR 15 and 20 the structures show a sub-linear trend of increasing density, going from 1.775 to 1.785 g/cm^3 and from 1.777 to 1.791 g/cm^3, for SAR 15 and 20 respectively. For ZSM-5C_37 it is reported a drop in density going from 1.784 g/cm^3 at RT to 1.779 g/cm^3 at 100 °C, with a consequent linear increase from 200 °C to 800 °C when the density reaches 1.788 g/cm^3. ZSM-5C_69 present a trend that is similar to ZSM-5C_37, with a starting density of 1.784 g/cm^3 with a drop to 1.781 g/cm^3 at 100 °C and then reaching 1.790 g/cm^3 at the end of the ramp. The trends for each sample are reported in figure 9
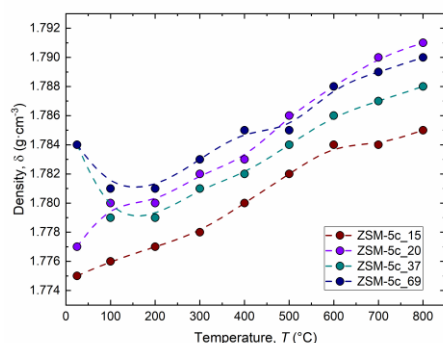
Figure 9. Evolution of density parameter with temperature for the four ZSM-5c samples.

4. Conclusions

The *in situ* synchrotron X-ray powder diffraction performed on ZSM-5 zeolites in their protonated form allowed to obtain important structural information of the most commonly exploited acid catalysts. Indeed, the knowledge of the structural response of the catalysts under operating conditions is a fundamental task to prevent and avoid unexpected phenomena limiting the catalytic activity. The results reported here confirm that the ZSM-5 zeolites maintain unchanged their crystallinity until the end of the thermal treatment, without significantly modifying their initial structural features, thus allowing to guarantee their full efficiency whether employed as acid catalysts. After TPA$^+$ decomposition and thermal activation, possible framework distortions occur, affecting the thermal regeneration and the efficiency of the ZSM-5 zeolite. The charge balance in ZSM-5 is achieved by the formation of Brønsted acid sites, which are responsible for the variation of the unit cell dimensions, mainly addressed by the T−O−T angle changes. Moreover, these variations reveal that the achieved bonding geometries are influenced by the initial Si/Al ratio. Furthermore, the T-O-T angles and the pore size geometries suggest a direct effect on the active site distribution within the pores/cavities. This information allows a better understanding of the catalytic activities and selectivities for specific chemical processes.

Supplementary Materials: The following supporting information can be downloaded at: www.mdpi.com/xxx/s1

Conflicts of Interest: Declare conflicts of interest or state "The authors declare no conflict of interest." Authors must identify and declare any personal circumstances or interest that may be perceived as inappropriately influencing the representation or interpretation of reported research results. Any role of the funders in the design of the study; in the collection, analyses or interpretation of data; in the writing of the manuscript; or in the decision to publish the results must be declared in this section. If there is no role, please state "The funders had no role in the design of the study; in

the collection, analyses, or interpretation of data; in the writing of the manuscript; or in the decision to publish the results".

References

1. Kerstens, D.; Smeyers, B.; Van Waeyenberg, J.; Zhang, Q.; Yu, J.; Sels, B.F. State of the Art and Perspectives of Hierarchical Zeolites: Practical Overview of Synthesis Methods and Use in Catalysis. Advanced Materials 2020, 32.

2. Li, Y.; Yu, J. Emerging Applications of Zeolites in Catalysis, Separation and Host–Guest Assembly. Nat Rev Mater 2021, 6.

3. Pérez-Botella, E.; Valencia, S.; Rey, F. Zeolites in Adsorption Processes: State of the Art and Future Prospects. Chem Rev 2022, 122.

4. Rimer, J.D. Rational Design of Zeolite Catalysts. Nat Catal 2018, 1.

5. Čejka, J.; Millini, R.; Opanasenko, M.; Serrano, D.P.; Roth, W.J. Advances and Challenges in Zeolite Synthesis and Catalysis. Catal Today 2020, 345, doi:10.1016/j.cattod.2019.10.021.

6. Ji, W.; Zhang, H.; Liu, S.; Wang, Z.; Deng, S. An Experimental Study on the Binary Hydrated Salt Composite Zeolite for Improving Thermochemical Energy Storage Performance. Renew Energy 2022, 194, doi:10.1016/j.renene.2022.06.024.

7. Zhang, R.; Ju, Y.; Wu, P.; Chen, J.; Lv, Z.; Zhang, Y.; Song, S.; Zhang, Z.; Ma, C.; Zhang, R.; et al. Efficiently Reducing Olefin Content of FCC Gasoline over ZSM-5 Zeolite Based Catalyst via Hydro-Upgrading. Catal Today 2022, 405–406, doi:10.1016/j.cattod.2022.08.003.

8. Mardiana, S.; Azhari, N.J.; Ilmi, T.; Kadja, G.T.M. Hierarchical Zeolite for Biomass Conversion to Biofuel: A Review. Fuel 2022, 309.

9. Chaturvedi, A.; Kundu, P.P. Co-Doped Zeolite-GO Nanocomposite as a High-Performance ORR Catalyst for Sustainable Bioelectricity Generation in Air-Cathode Single-Chambered Microbial Fuel Cells. ACS Appl Mater Interfaces 2022, doi:10.1021/acsami.2c07638.

10. Gao, S.; Wang, S.; Hu, P.; Wang, J.; Sun, Y.; Ma, Z. Performance of Sorption Thermal Energy Storage in Zeolite Bed Reactors: Analytical Solution and Experiment. J Energy Storage 2023, 64, doi:10.1016/j.est.2023.107154.

11. Boer, D.G.; Čiliak, D.; Langerak, J.; Bakker, B.; Pescarmona, P.P. Binderless SAPO-34 Beads for Selective CO2 Adsorption. Sustainable Chemistry for Climate Action 2023, 2, 100026, doi:https://doi.org/10.1016/j.scca.2023.100026.

12. Velty, A.; Corma, A. Advanced Zeolite and Ordered Mesoporous Silica-Based Catalysts for the Conversion of CO2 to Chemicals and Fuels. Chem Soc Rev 2023, 52.

13. Mancinelli, M.; Stevanin, C.; Ardit, M.; Chenet, T.; Pasti, L.; Martucci, A. PFAS as Emerging Pollutants in the Environment: A Challenge with FAU Type and Silver-FAU Exchanged Zeolites for Their Removal from Water. J Environ Chem Eng 2022, 10, doi:10.1016/j.jece.2022.108026.

14. Mahdavi Far, R.; Van der Bruggen, B.; Verliefde, A.; Cornelissen, E. A Review of Zeolite Materials Used in Membranes for Water Purification: History, Applications, Challenges and Future Trends. Journal of Chemical Technology and Biotechnology 2022, 97.

15. Panasenko, A.E.; Shichalin, O.O.; Yarusova, S.B.; Ivanets, A.I.; Belov, A.A.; Dran'kov, A.N.; Azon, S.A.; Fedorets, A.N.; Buravlev, I.Y.; Mayorov, V.Y.; et al. A Novel Approach for Rice Straw Agricultural Waste Utilization: Synthesis of Solid Aluminosilicate Matrices

for Cesium Immobilization. Nuclear Engineering and Technology 2022, 54, doi:10.1016/j.net.2022.04.005.

16. Kausar, A.; Ahmad, I.; Zhu, T.; Shahzad, H.; Eisa, M.H. Exigency for the Control and Upgradation of Indoor Air Quality—Forefront Advancements Using Nanomaterials. Pollutants 2023, 3, doi:10.3390/pollutants3010011.

17. Ziejewska, C.; Grela, A.; Łach, M.; Marczyk, J.; Hordyńska, N.; Szechyńska-Hebda, M.; Hebda, M. Eco-Friendly Zeolites for Innovative Purification of Water from Cationic Dye and Heavy Metal Ions. J Clean Prod 2023, 406, 136947, doi:https://doi.org/10.1016/j.jclepro.2023.136947.

18. Vezzalini, G.; Quartieri, S.; Galli, E.; Alberti, A.; Cruciani, G.; Kvick, Å. Crystal Structure of the Zeolite Mutinaite, the Natural Analog of ZSM-5. Zeolites 1997, 19, doi:10.1016/S0144-2449(97)00124-3.

19. Olson, D.H.; Kokotailo, G.T.; Lawton, S.L.; Meier, W.M. Crystal Structure and Structure-Related Properties of ZSM-5. Journal of Physical Chemistry 1981, 85, doi:10.1021/j150615a020.

20. Kokotailo, G.T.; Lawton, S.L.; Olson, D.H.; Meier, W.M. Structure of Synthetic Zeolite ZSM-5. Nature 1978, 272, doi:10.1038/272437a0.

21. Baerlocher, C.; McCusker, L.B.; Olson, D.H. Atlas of Zeolite Framework Types, 6th Edition; 2007;

22. Van Koningsveld, H.; Jansen, J.C. Single Crystal Structure Analysis of Zeolite H-ZSM-5 Loaded with Naphthalene. Microporous Materials 1996, 6, doi:10.1016/0927-6513(95)00097-6.

23. Van Koningsveld, H.; Van Bekkum, H.; Jansen, J.C. On the Location and Disorder of the Tetrapropylammonium (TPA) Ion in Zeolite ZSM-5 with Improved Framework Accuracy. Acta Crystallographica Section B 1987, 43, doi:10.1107/S0108768187098173.

24. Van Koningsveld, H. High-temperature (350 K) Orthorhombic Framework Structure of Zeolite H-ZSM-5. Acta Crystallographica Section B 1990, 46, doi:10.1107/S0108768190007522.

25. Kamiya, N.; Oshiro, T.; Tan, S.; Nishi, K.; Yokomori, Y. Adsorption Process of Phenol on Silicalite-1 and Crystal Structure of Phenol8.0-Silicalite-1 Using a Single Crystal X-Ray Diffraction Method. Microporous and Mesoporous Materials 2013, 169, doi:10.1016/j.micromeso.2012.11.006.

26. Nishi, K.; Hidaka, A.; Yokomori, Y. Structure of Toluene6.4-ZSM-5 and the Toluene Disproportionation Reaction on ZSM-5. Acta Crystallogr B 2005, 61, doi:10.1107/S0108768105003186.

27. Reck, G.; Marlow, F.; Kornatowski, J.; Hill, W.; Caro, J. Structure of Dipole Chains in an MFI Type Molecular Sieve. Journal of Physical Chemistry 1996, 100, doi:10.1021/jp950454w.

28. Klein, H.; Fuessa, H.; Ernst, S.; Weitkamp, J. Localization of Naphthalenes in Zeolite HZSM-5 by X-Ray Powder Diffraction and Molecular Mechanics Calculation. Microporous Materials 1994, 3, doi:10.1016/0927-6513(94)00037-9.

29. van Koningsveld, H.; Tuinstra, F.; Jansen, J.C.; van Bekkum, H. On the Preparation of a Monoclinic (Nearly) Single Crystal of Zeolite HZSM-5. Zeolites 1989, 9, doi:10.1016/0144-2449(89)90035-3.

30. Ardit, M.; Martucci, A.; Cruciani, G. Monoclinic Orthorhombic Phase Transition in ZSM 5 Zeolite: Spontaneous Strain Variation and Thermodynamic Properties. Journal of Physical Chemistry C 2015, 119, doi:10.1021/acs.jpcc.5b00900.

31. Ardit, M.; Martucci, A.; Pasti, L.; Rodeghero, E.; Beltrami, G.; Cruciani, G. Organic Guests within a Ferroelastic Host: The Case of High Silica Zeolite ZSM-5. Journal of Physical Chemistry C 2018, 122, doi:10.1021/acs.jpcc.8b00686.

32. Ji, Y.; Yang, H.; Yan, W. Strategies to Enhance the Catalytic Performance Of. Catalysts 2017, 7.

33. Lok, C.M.; Van Doorn, J.; Aranda Almansa, G. Promoted ZSM-5 Catalysts for the Production of Bio-Aromatics, a Review. Renewable and Sustainable Energy Reviews 2019, 113.

34. Ding, Y.L.; Wang, H.Q.; Xiang, M.; Yu, P.; Li, R.Q.; Ke, Q.P. The Effect of Ni-ZSM-5 Catalysts on Catalytic Pyrolysis and Hydro-Pyrolysis of Biomass. Front Chem 2020, 8.

35. Alotibi, M.F.; Alshammari, B.A.; Alotaibi, M.H.; Alotaibi, F.M.; Alshihri, S.; Navarro, R.M.; Fierro, J.L.G. ZSM-5 Zeolite Based Additive in FCC Process: A Review on Modifications for Improving Propylene Production. Catalysis Surveys from Asia 2020, 24.

36. Dai, W.; Zhang, L.; Liu, R.; Wu, G.; Guan, N.; Li, L. Plate-Like ZSM-5 Zeolites as Robust Catalysts for the Cracking of Hydrocarbons. ACS Appl Mater Interfaces 2022, 14, doi:10.1021/acsami.1c23614.

37. Mohammadi, L.; Hosseinifard, M.; Vaezi, M.R.; Rostamnia, S. Stabilization of Copper Nanoparticles onto the Double Schiff-Base-Functionalized ZSM-5 for A3 Coupling Reaction Catalysis Aimed under Mild Conditions. RSC Adv 2023, 13, doi:10.1039/d2ra07700k.

38. Martucci, A.; Rodeghero, E.; Pasti, L.; Bosi, V.; Cruciani, G. Adsorption of 1,2-Dichloroethane on ZSM-5 and Desorption Dynamics by in Situ Synchrotron Powder X-Ray Diffraction. Microporous and Mesoporous Materials 2015, 215, doi:10.1016/j.micromeso.2015.05.035.

39. Rodeghero, E.; Pasti, L.; Sarti, E.; Cruciani, G.; Bagatin, R.; Martucci, A. Temperature-Induced Desorption of Methyl Tert-Butyl Ether Confined on ZSM-5: An in Situ Synchrotron XRD Powder Diffraction Study. Minerals 2017, 7, doi:10.3390/min7030034.

40. Pasti, L.; Rodeghero, E.; Sarti, E.; Bosi, V.; Cavazzini, A.; Bagatin, R.; Martucci, A. Competitive Adsorption of VOCs from Binary Aqueous Mixtures on Zeolite ZSM-5. RSC Adv 2016, 6, doi:10.1039/c6ra08872d.

41. Pasti, L.; Rodeghero, E.; Beltrami, G.; Ardit, M.; Sarti, E.; Chenet, T.; Stevanin, C.; Martucci, A. Insights into Adsorption of Chlorobenzene in High Silica MFI and FAU Zeolites Gained from Chromatographic and Diffractometric Techniques. Minerals 2018, 8, doi:10.3390/min8030080.

42. Marinkovic, B.A.; Jardim, P.M.; Saavedra, A.; Lau, L.Y.; Baehtz, C.; de Avillez, R.R.; Rizzo, F. Negative Thermal Expansion in Hydrated HZSM-5 Orthorhombic Zeolite. Microporous and Mesoporous Materials 2004, 71, doi:10.1016/j.micromeso.2004.03.023.

43. Sen, S.; Wusirika, R.R.; Youngman, R.E. High Temperature Thermal Expansion Behavior of H[Al]ZSM-5 Zeolites: The Role of Brønsted Sites. Microporous and Mesoporous Materials 2006, 87, doi:10.1016/j.micromeso.2005.08.010.

44. Migliori, M.; Aloise, A.; Giordano, G. Methanol to Dimethylether on H-MFI Catalyst: The Influence of the Si/Al Ratio on Kinetic Parameters. Catal Today 2014, 227, doi:10.1016/j.cattod.2013.09.033.

45. Frusteri, F.; Bonura, G.; Cannilla, C.; Drago Ferrante, G.; Aloise, A.; Catizzone, E.; Migliori, M.; Giordano, G. Stepwise Tuning of Metal-Oxide and Acid Sites of CuZnZr-MFI Hybrid Catalysts for the Direct DME Synthesis by CO2 Hydrogenation. Appl Catal B 2015, 176–177, doi:10.1016/j.apcatb.2015.04.032.

46.   Toby, B.H. EXPGUI , a Graphical User Interface for GSAS. J Appl Crystallogr 2001, 34, 210–213, doi:10.1107/S0021889801002242.

47.   Larson, A.C.; Von Dreele, R.B. General Structure Analysis System (GSAS), Los. Alamos National Laboratory Report LAUR 86-748; 2004;

48.   Van Koningsveld, H.; Tuinstra, F.; Van Bekkum, H.; Jansen, J.C. The Location of P-xylene in a Single Crystal of Zeolite H-ZSM-5 with a New, Sorbate-induced, Orthorhombic Framework Symmetry. Acta Crystallographica Section B 1989, 45, doi:10.1107/S0108768189004519.

49.   Shannon, R.D. Revised Effective Ionic Radii and Systematic Studies of Interatomic Distances in Halides and Chalcogenides. Acta Crystallographica Section A 1976, 32, doi:10.1107/S0567739476001551.

50.   Arletti, R.; Cruciani, G.; Ferraris, G. Section 7.14.2. Mineral Physics through in Situ Powder-Diffraction Experiments. In International Tables for Crystallography ; Gilmore, C.J., Kaduk, J.A., Schenk, H., Eds.; Wiley, 2019; Vol. H, pp. 886–889.

51.   Fei, Y. Thermal Expansion. In Mineral Physics & Crystallography: A Handbook of Physical Constants,; Ahrens, T.J., Ed.; American Geophysical Union: Washington, D. C., 1995; Vol. Volume 2, pp. 29–44.

52.   Angel, R.J.; Gonzalez-Platas, J.; Alvaro, M. EosFit7c and a Fortran Module (Library) for Equation of State Calculations. Zeitschrift fur Kristallographie 2014, 229, doi:10.1515/zkri-2013-1711.

53.   Bhange, D.S.; Ramaswamy, V. Negative Thermal Expansion in Silicalite-1 and Zirconium Silicalite-1 Having MFI Structure. Mater Res Bull 2006, 41, doi:10.1016/j.materresbull.2005.12.002.

54.   Milanesio, M.; Artioli, G.; Gualtieri, A.F.; Palin, L.; Lamberti, C. Template Burning inside TS-1 and Fe-MFI Molecular Sieves: An in Situ XRPD Study. J Am Chem Soc 2003, 125, doi:10.1021/ja037229+.